


Article

Ferrocene Formic Acid Surface Modified Ni(OH)₂ for Highly Efficient Alkaline Oxygen Evolution

Guo-Ping Shen ¹, Ruo-Yao Fan ¹, Bin Dong ^{1,*} and Bo Chen ^{2,*} 

¹ State Key Laboratory of Heavy Oil Processing, College of Chemistry and Chemical Engineering, University of Petroleum (East China), Qingdao 266580, China

² Department of Chemistry, City University of Hong Kong, Kowloon, Hong Kong, China

* Correspondence: dongbin@upc.edu.cn (B.D.); bchen005@e.ntu.edu.sg (B.C.)

Abstract: FeNi-based hybrid materials are among the most representative catalysts for alkaline oxygen evolution reaction (OER), but the modulation of their surface atoms to achieve the optimal catalytic properties is still a big challenge. Here, we report the surface modification of Ni(OH)₂/nickel foam (NF)-based electrocatalyst with a trace amount of ferrocene formic acid (FFA) (FFA-Ni(OH)₂/NF) for highly efficient OER. Owing to the strong electron interaction and synergistic effects of Fe-Ni heteroatoms, FFA-Ni(OH)₂/NF exhibits an overpotential of 311 mV at a current density of 100 mA cm⁻². Impressively, the overpotential of FFA-Ni(OH)₂/NF at 100 mA cm⁻² is 108 mV less than that of bulk phase doped Ni/FFA(OH)₂/NF, demonstrating the surprising effect of heteroatomic surface modification. In addition, by introducing a small amount of surface modifier into the electrolyte, the weak surface reconstruction process in the electrochemical process can be fully utilized to achieve obvious modification effects. Therefore, this work fully proves the feasibility of improving catalytic activities of FeNi-based catalysts by modifying surface heterogeneous atom pairs.

Keywords: oxygen evolution reaction (OER); surface modification; Ni(OH)₂; FeNi-based catalysts



Citation: Shen, G.-P.; Fan, R.-Y.;

Dong, B.; Chen, B. Ferrocene Formic Acid Surface Modified Ni(OH)₂ for Highly Efficient Alkaline Oxygen Evolution. *Crystals* **2022**, *12*, 1404. <https://doi.org/10.3390/cryst12101404>

Academic Editor: Leonid Kustov

Received: 29 August 2022

Accepted: 30 September 2022

Published: 4 October 2022

Publisher's Note: MDPI stays neutral with regard to jurisdictional claims in published maps and institutional affiliations.



Copyright: © 2022 by the authors. Licensee MDPI, Basel, Switzerland. This article is an open access article distributed under the terms and conditions of the Creative Commons Attribution (CC BY) license (<https://creativecommons.org/licenses/by/4.0/>).

1. Introduction

Developing sustainable green energy is a key way to realize a low-carbon transition [1,2]. At present, the development of main renewable green energy sources, including solar energy, tidal energy, wind energy, and geothermal energy, are severely limited by their intermittency, instability, and regionalism [3–5]. Hydrogen, by contrast, has a high energy density and good sustainability and is emerging as the latest star in the third energy revolution of the world [6–9].

Compared with traditional industrial hydrogen production, water electrolysis is a more ideal way for hydrogen production because of its advantages, such as being sustainable and pollution-free [10–12]. However, the efficiency of hydrogen production from water electrolysis is severely limited by the oxygen evolution reaction (OER) of four-electron transfer that occurs slowly at the anode [13–16]. At present, the most widely-used catalysts for OER are precious metals and their derivatives such as RuO₂ and IrO₂, which suffer from their high price and rare reserves [17–21]. It is reported that the well-designed FeNi-based hybrid catalytic materials in an alkaline environment have superior OER performance comparable to that of precious metals [22–26]. However, the key problem limiting the development of FeNi-based hybrid catalysts, especially FeNiO_xH_y, is that under the action of oxidation current, the strong oxidation and reconstruction of the surface of catalysts, lead to the loss of active sites and stability attenuation [27,28]. Therefore, the design and synthesis of FeNi-based catalytic materials with heterogeneous catalytic surfaces for the long-term OER is still a research hotspot.

Through accidental or intentional Fe doping or incorporation, the OER activity of nickel/cobalt-based electrocatalysts can be greatly increased, which is called the “Fe effect” [29–31]. Many researchers have discovered this phenomenon, but few have applied it

to the synthesis and development of Fe-Ni and Fe-Co-based bimetallic composites. Furthermore, our previous work has shown that catalytic surfaces rich in nickel and low in iron are more conducive to the bonding of heterogeneous atoms to maintain the long-term stability of FeNi-based hybrid materials [32].

Herein, we synthesized trace ferrocene formic acid (FFA) modified Ni(OH)₂ hybrid catalyst by a simple electrochemical activation method to provide excellent OER performance in an alkaline solution. Due to the unique heteroatomic bond cooperation assisted by electrochemistry, the introduction of a small amount of ferrocene formic acid in the electrolyte can significantly improve the reaction current and oxygen evolution efficiency, indicating that it has a good modification effect on Ni(OH)₂ catalytic surface. Meanwhile, after ferrocene formic acid was introduced, the solid electronic interactions between Ni and Fe might change the electronic structure of Ni(OH)₂ to provide suitable intermediate adsorption energy. Impressively, the OER activity of Ni/FFA(OH)₂/NF is far inferior to that of FFA-Ni(OH)₂/NF.

2. Experimental Section

2.1. Chemicals

Ni(NO₃)₂·6H₂O (AR), C₁₁H₁₀FeO₂ (AR), and C₃H₇NO (DMF) (AR) were purchased from Macklin (Shanghai, China). We used standard analytical pure KOH (purchased from Sinopharm Chemical Reagent Co., Ltd., Shanghai, China) to prepare the electrolyte. The content of Fe in this KOH is less than 0.001%. Nickel foams (NFs) were ultrasonically cleaned in acetone, hydrochloric acid (1 mol L⁻¹), and ethanol for 30 min. In this experiment, all electrolytes are prepared with specially purified ultrapure water to avoid any impurities. The models of electric heating constant temperature blast drying oven, muffle furnace, and tube furnace are DGG-90030G, KSL-1200X, and ZL-2011-2-0389859.8, respectively.

2.2. Synthesis of the Ni(OH)₂/NF

The growth solution contains ammonium fluoride (3 mmol), nickel nitrate (3 mmol), urea (10 mmol), and deionized water (40 mL) [33,34]. The prepared solution was then added to the reactor including a piece of NF (2 cm × 2 cm), and then heated at 100 °C for 12 h. Finally, a color transition of NF from silver-gray to light green can be observed.

2.3. Synthesis of the FFA-Ni(OH)₂/NF

FFA-Ni(OH)₂ was obtained by rapid electrochemical activation. First, Ni(OH)₂/NF was activated to a stable state by linear sweep voltammetry (LSV) (5 mV s⁻¹, 0–0.7 V vs. SCE, 5 cycles). Then, ferrocene formic acid solution (0.05 mol L⁻¹) was added to the electrolyte drop by drop and stirred evenly. At the same time, LSV scanning was continued until stable. Finally, about 40 μL ferrocene formic acid solution was added until achieving the optimum activity. Finally, the obtained FFA-Ni(OH)₂/NF catalyst was washed with deionized water.

2.4. Synthesis of the Ni/FFA(OH)₂/NF

The synthetic method of Ni/FFA(OH)₂/NF is almost the same as that of Ni(OH)₂/NF, except that the growth solution is replaced with 10 mL 0.05 mol L⁻¹ ferrocene formic acid solution, nickel nitrate (3 mmol), urea (10 mmol) and deionized water (40 mL).

2.5. Characterization

X-ray diffraction (XRD, Rigaku D/MAX-2500PC) with Cu Kα, λ = 1.54 Å was used to investigate the crystal phase-related information of the obtained catalysts. The instrument models of scanning electron microscopy (SEM) and transmission electron microscopy (TEM) are Hitachi S-4800 and FEI Tecnai G20, respectively. The SEM-energy dispersive spectrometer (EDS) was used to analyze the detailed elemental composition of the catalyst. X-ray photoelectron spectroscopy (XPS) was tested on a Thermo Fisher Scientific II spectrometer using an Al Kα source.

2.6. Electrochemical Measurements

The electrochemical activities of catalysts were tested with a Gamry Reference 600 workstation in 1 M KOH electrolyte. In a typical three-electrode system, the working, counter, and reference electrodes are catalysts on NF, platinum sheet, and calomel electrode, respectively. Specifically, the LSV sweep is set at 5 mV s^{-1} ; the test voltage and frequency ranges of electrochemical impedance spectroscopy (EIS) are 0.45 V vs. SCE and 10^5 –0.1 Hz; the current density for the chronopotentiometry method is 200 mA cm^{-2} . The electrochemical active surface areas (ECSAs) of electrocatalysts were measured by cyclic voltammetry (CV). Test voltage range was set as 1.35–1.45 V vs. RHE and sweep speeds were set as 20, 40, 60, 80, and 100 mV s^{-1} . Their electrochemical double-layer capacitances (C_{dl}) were obtained from the change rate of voltage with sweep speed. According to the formula $\text{ESCA} = C_{dl}/C_s$ ($C_s = 0.04 \text{ mF}$), the corresponding ECSA of each sample can be obtained.

3. Results and Discussion

Figure 1 shows the detailed synthesis pathway of trace ferrocene formic acid (FFA)-modified $\text{Ni}(\text{OH})_2$ electrocatalyst (named $\text{FFA-Ni}(\text{OH})_2/\text{NF}$), including a one-step hydrothermal reaction and simple electrochemical activation process. It has been reported that $\text{Ni}(\text{OH})_2$ has a special bonding effect for Fe ions, and the electrochemical reconstruction process of OER can promote the interaction of Fe-Ni heteroatomic pairs [24,25]. The XRD peaks of pure Ni foam are consistent with the characteristic peaks of standard Ni (00-003-1051) (Figure S1, see Supplementary Materials). $\text{Ni}(\text{OH})_2$ synthesized by hydrothermal reaction has a mixed crystal phase structure. As shown in Figure 2a, XRD peaks of $\text{Ni}(\text{OH})_2/\text{NF}$ correspond to the standard peaks of $\alpha\text{-Ni}(\text{OH})_2$ (00-038-0715) and $\beta\text{-Ni}(\text{OH})_2$ (01-074-2075). After the surface treatment with ferrocene formic acid, the original crystal structure of $\text{Ni}(\text{OH})_2$ was basically retained, and the characteristic peaks of $\text{Fe}(\text{OH})_3$ were also detected. This indicates that a tiny proportion of ferrocene is electro-activated to form $\text{Fe}(\text{OH})_3$ after electrochemical action due to the particular interaction of Fe-Ni heteroatoms. In alkaline environments, OH intermediates can be adsorbed to Ni-Fe sites by terminal bonding or bridging to form heteroatomic bonds—Fe-O-Ni, which can be pivotal catalytic sites with high OER activity [35,36].

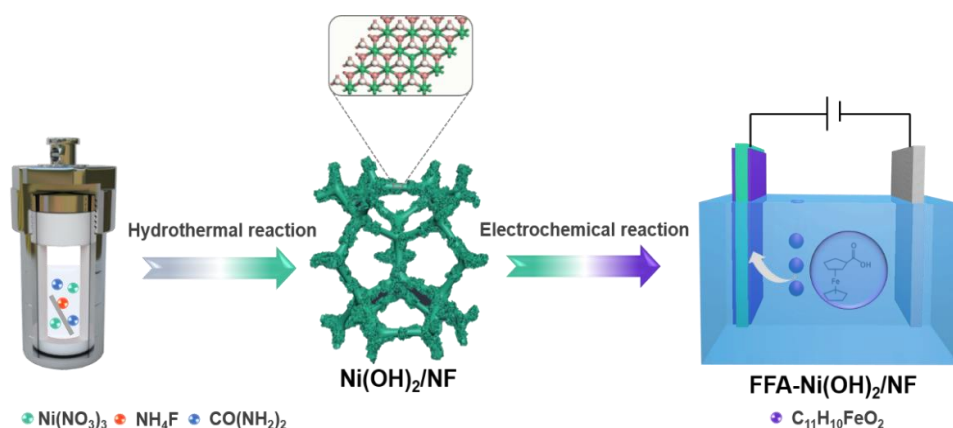


Figure 1. Schematic diagram of the preparation of $\text{FFA-Ni}(\text{OH})_2/\text{NF}$.

In addition, the near-surface species composition and elemental valence states of all electrocatalysts were characterized by XPS. Characteristic peaks of Ni, O, and Fe appear in the full-range spectral data of $\text{FFA-Ni}(\text{OH})_2/\text{NF}$ (Figure 2b), which is consistent with the XRD data mentioned above. In detail, the Ni 2p peaks of $\text{FFA-Ni}(\text{OH})_2/\text{NF}$ could be divided into four peaks: Ni 2p_{3/2} (854.83 eV), Ni 2p_{1/2} (877.42 eV), Sat1 (860.51 eV) and Sat2 (878.40 eV) (Figure 2c). For the Ni 2p spectrum of $\text{Ni}(\text{OH})_2/\text{NF}$, four similar peaks are located at 855.23, 861.03, 873.03, and 878.94 eV, respectively. A detailed comparison shows that the peak of Ni 2p_{3/2} of $\text{FFA-Ni}(\text{OH})_2/\text{NF}$ is offset by 0.4 eV relative to $\text{Ni}(\text{OH})_2/\text{NF}$, indicating an intense electron interaction between the introduced Fe and Ni.

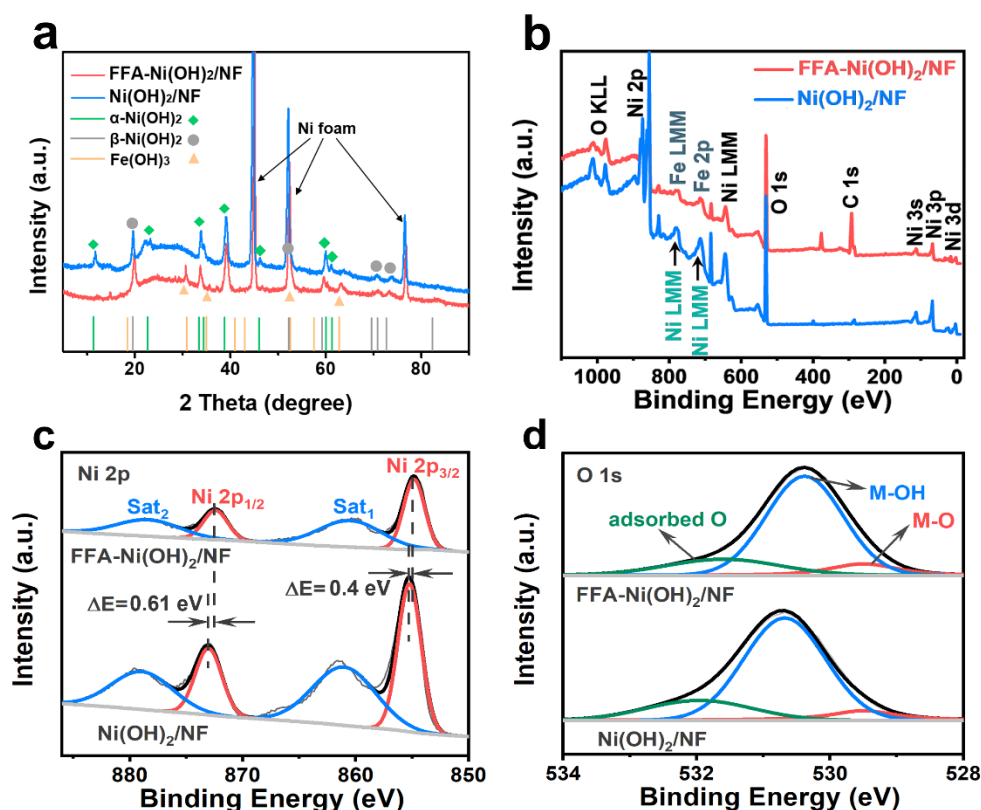


Figure 2. (a) Typical XRD patterns of Ni(OH)₂/NF and FFA-Ni(OH)₂/NF. (b) XPS spectra of FFA-Ni(OH)₂/NF (red) and Ni(OH)₂/NF (blue). (c) Ni 2p and (d) O 1s spectra of FFA-Ni(OH)₂/NF and Ni(OH)₂/NF.

In addition, the O 1s of FFA-Ni(OH)₂/NF and Ni(OH)₂/NF can be divided into three peaks corresponding to O-M (520 eV), O-H (531 eV), and adsorbed oxygen (532 eV) (Figure 2d). Compared with Ni(OH)₂/NF, the M-O peak of FFA-Ni(OH)₂/NF also exhibits a 0.3 eV shift, which is also due to the electron interaction of Fe-Ni heteroatom pairs. The 2p profile of Fe is shown in Figure S2. The peak of Fe is puzzling due to the interference of the strong Auger peak of Ni. This may also be caused by too little Fe content on the surface of FFA-Ni(OH)₂/NF.

The surface morphology information of electrocatalysts can be obtained from SEM. The surface of the pure NF is smooth, which is not conducive to the exposure of the catalytic active site and the direct application of the catalytic process (Figure S3). However, NF is more suitable for dispersion substrate because of its complex pore structure. In Figure 3a, the Ni(OH)₂/NF prepared by the hydrothermal method presents a flower-like three-dimensional structure with the aggregation of ultra-thin nanosheets. Polygonal ultra-thin nanosheets are more conducive to providing a large specific surface area and rich active sites (Figure 3d). Moreover, the interspaces formed by the cross-linking of nanosheets can provide a large number of gas transport channels to promote oxygen desorption. The surface elemental distribution of Ni(OH)₂/NF is demonstrated in Figure S4, and it can be found that Ni and O are distributed uniformly on the surface of the nanosheet. As we can see in Figure 3b, after ferrocene formic acid surface modification and electrochemical activation, FFA-Ni(OH)₂/NF can still maintain the morphology of flower-like nanosheet clusters, indicating that the main structure of the original precursor will not be damaged by FFA modification. More notably, compared with Ni(OH)₂/NF, FFA-Ni(OH)₂/NF has a thinner and more uniform nanosheet-like structure (Figure 3e), which may be more conducive to the exposure of active catalytic sites and transport of gas. In addition, FFA was added to the growth solution to prepare bulk phase doped Ni/FFA(OH)₂/NF, as shown in Figure 3c. It is not difficult to find that Ni/FFA(OH)₂/NF does not possess the flower-like morphology

of nanosheet aggregation, which may be because the addition of FFA hinders the crystal growth of $\text{Ni}(\text{OH})_2$. In Figure 3f, $\text{Ni}/\text{FFA}(\text{OH})_2/\text{NF}$ has a spongy porous structure, which is harmful to providing a large specific surface area and abundant active sites. To better reveal the influence of the morphology of electrocatalysts on the ECSA, we carried out CV tests on all samples (Figure S5). The results show that $\text{FFA-Ni}(\text{OH})_2/\text{NF}$ (37.18 mF cm^{-2}) has the largest C_{dl} compared with $\text{Ni}(\text{OH})_2/\text{NF}$ (23.36 mF cm^{-2}), $\text{Ni}/\text{FFA}(\text{OH})_2/\text{NF}$ (30.55 mF cm^{-2}). The ECSAs of $\text{FFA-Ni}(\text{OH})_2/\text{NF}$, $\text{Ni}/\text{FFA}(\text{OH})_2/\text{NF}$, and $\text{Ni}(\text{OH})_2/\text{NF}$ are 929.50 , 763.75 , and 584.00 cm^{-2} , respectively (according to the formula: $\text{ECSA} = C_{\text{dl}}/C_s$). The results of the electrochemical test are consistent with SEM characterizations. SEM-Mapping results further showed that Fe, Ni, and O contained in $\text{FFA-Ni}(\text{OH})_2/\text{NF}$ were uniformly distributed, indicating that the electrochemical activation process could achieve uniform Fe dispersion. The content of the Fe element is really low (atomic content as low as 0.22%, Figure S6), indicating that a small amount of FFA can provide a significant modification effect.

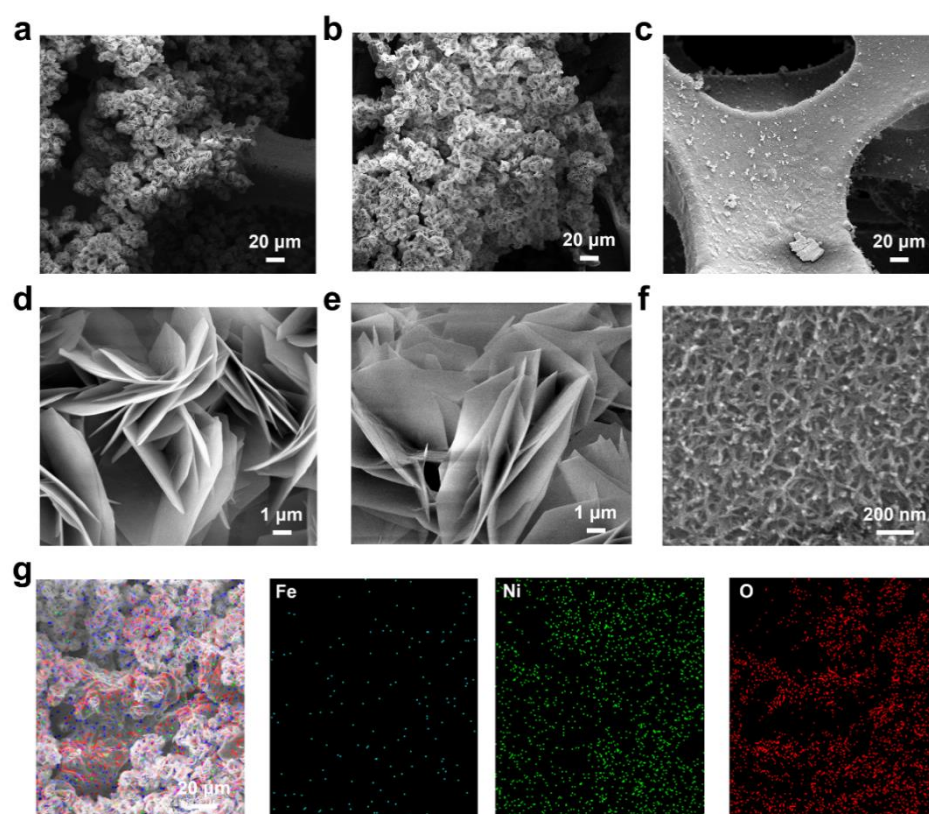


Figure 3. SEM images of $\text{Ni}(\text{OH})_2/\text{NF}$ (a,d), $\text{FFA-Ni}(\text{OH})_2/\text{NF}$ (b,e), and $\text{Ni}/\text{FFA}(\text{OH})_2/\text{NF}$ (c,f). (g) SEM image and EDX elemental mappings of $\text{FFA-Ni}(\text{OH})_2/\text{NF}$.

To further highlight the enhanced catalytic effect of surface modification, detailed electrochemical characterizations were carried out for all electrocatalysts in 1 M KOH. In Figure 4a, compared with pure $\text{Ni}(\text{OH})_2/\text{NF}$, the alkaline OER activity of $\text{Ni}(\text{OH})_2$ modified by FFA was significantly improved. This may be due to the strong electron interaction and synergistic catalytic effects of Fe-Ni heteroatoms on the catalytic surface. Meanwhile, a small amount of ferrocene formic acid solution was added to the growth solution to synthesize bulk doped $\text{Ni}(\text{OH})_2$ ($\text{Ni}/\text{FFA}(\text{OH})_2/\text{NF}$) as the contrast sample.

As expected, the OER properties of $\text{Ni}/\text{FFA}(\text{OH})_2/\text{NF}$ are not ideal. Compared with $\text{Ni}(\text{OH})_2/\text{NF}$, its overpotential reduces by only 30 mV, while $\text{FFA-Ni}(\text{OH})_2/\text{NF}$ reduces by 138 mV at 100 mA cm^{-2} (Figure 4b). The excellent modification effect of ferrocene formic acid surface modification can be well proved. In Figure 4g, the electrocatalysts in this work have better performances over several previously reported Fe-Ni-based OER catalysts

(Table S1). More importantly, FFA-Ni(OH)₂/NF exhibits an overpotential of 350 mV at a current density of 300 mA cm⁻², which is 240 mV less than Ni(OH)₂/NF. OER reaction kinetics of electrocatalysts can be reflected by the Tafel slope. As we can see in Figure 4c, FFA-Ni(OH)₂/NF has the smallest Tafel slope (77.68 mV dec⁻¹), indicating that it has improved OER reaction kinetics. In addition, the system resistance (R_s) and charge transfer resistance (R_{ct}) of the catalytic system were studied by electrochemical impedance spectroscopy (EIS). Our results show that the system resistances of NF, Ni(OH)₂/NF, Ni/FFA(OH)₂/NF, and FFA-Ni(OH)₂/NF are similar, but the R_{ct} of FFA-Ni(OH)₂/NF decreases nearly 100 times, which indicates that the electron transfer rate of the catalytic surface is obviously accelerated after surface modification with FFA (Figure 4d). This is probably because of the presence of conjugated electrons in the organic match, which makes the conductivity of the material significantly improved. In conclusion, FFA-Ni(OH)₂/NF exhibits surprising OER performances thanks to the electron interaction of Fe-Ni heteroatomic pairs, the surface modification effect of FFA, and the stereoscopic flower structure.

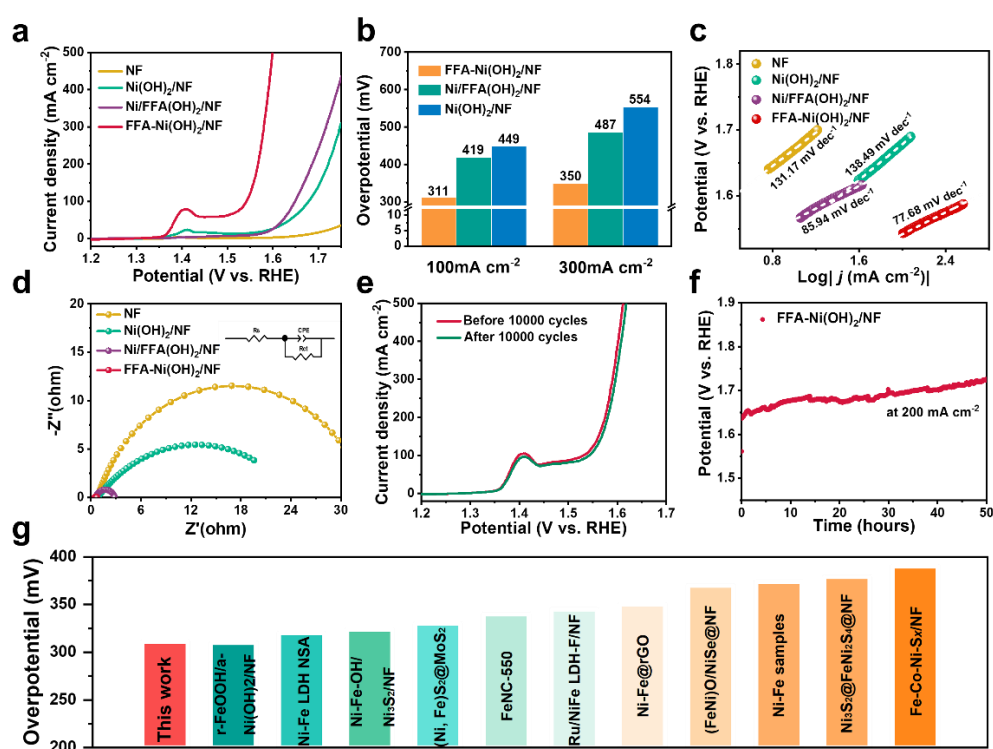


Figure 4. (a) LSV, (b) overpotential, (c) Tafel, and (d) EIS of FFA-Ni(OH)₂/NF, Ni(OH)₂/NF, Ni/FFA(OH)₂/NF, and NF. (e) LSV of FFA-Ni(OH)₂/NF before and after 10,000 CV cycles. (f) The chronopotentiometry (CP) test at 200 mA cm⁻² of FFA-Ni(OH)₂/NF in 1 M KOH solution. (g) Comparison of the overpotentials of the catalyst in this work and the previously reported Fe-Ni-based OER catalysts.

In addition, the stability test of FFA-Ni(OH)₂/NF was explored in detail. As exhibited in Figure 4e, after 10,000 cycles of CV, the LSV profiles of FFA-Ni(OH)₂/NF basically coincide, indicating that it has excellent cycling stability. More importantly, after 50 h of stability testing, the reaction current of FFA-Ni(OH)₂/NF did not decay significantly, proving that it also had preminent long-term stability (Figure 4f). Due to the interaction of abundant conjugated electron pairs, organic iron may be more conducive to Fe site stabilization than inorganic Fe salt. Importantly, the overpotential of the catalyst in this work is comparable to those of previously reported Fe-Ni-based OER catalysts (Figure 4g and Table S1) [37–47]. Therefore, the performance and stability of FFA-Ni(OH)₂/NF will meet the requirements of OER catalysts for future industrial applications.

4. Conclusions

In summary, FFA-Ni(OH)₂/NF synthesized by electrochemical activation and surface modification of FFA exhibited excellent OER performances in alkaline solution. Electrochemical tests revealed that FFA-Ni(OH)₂/NF only required an overpotential of 311 mV at 100 mA cm⁻², which was 138 mV less than that of Ni(OH)₂/NF. Moreover, the electrocatalytic activities of Ni(OH)₂/NF are stable after 10,000 cycles and up to 50 h of durability test. The excellent and comprehensive properties of FFA-Ni(OH)₂/NF may come from the following two aspects: (1) the strong electronic interaction of Fe-Ni heteroatom pairs positively regulates the binding energy of oxygen-containing intermediates. (2) the flower-like structure of Ni(OH)₂/NF composed of ultrathin nanosheets is well-maintained after micro FFA surface modification. Our research proves that surface modification is an effective way to achieve the performance enhancement of FeNi-based electrocatalysts.

Supplementary Materials: The following supporting information can be downloaded at: <https://www.mdpi.com/article/10.3390/cryst12101404/s1>, Figure S1: XRD of Ni foam; Figure S2: Fe 2p of FFA-Ni(OH)₂/NF; Figure S3: SEM images of NF; Figure S4: SEM-Mappings of Ni(OH)₂/NF; Figure S5: CVs of (a) FFA-Ni(OH)₂/NF, (b) Ni/FFA(OH)₂/NF, and (c) Ni(OH)₂/NF (at 1.35–1.45 V vs. RHE). (d) C_{dl} of FFA-Ni(OH)₂/NF, Ni/FFA(OH)₂/NF and Ni(OH)₂/NF; Figure S6: The surface element content statistics of FFA-Ni(OH)₂/NF; Table S1: Comparison of the overpotential between the catalyst in this work and the previously reported Fe-Ni based OER electrocatalysts [37–47].

Author Contributions: Methodology, G.-P.S.; data curation, G.-P.S. and R.-Y.F.; formal analysis, G.-P.S. and R.-Y.F.; investigation, B.D.; resources, G.-P.S.; writing—original draft preparation, G.-P.S., R.-Y.F., B.D. and B.C.; writing—review and editing, G.-P.S., R.-Y.F., B.D. and B.C.; supervision, B.D. and B.C.; funding acquisition, B.D. All authors have read and agreed to the published version of the manuscript.

Funding: This work is financially supported by the National Natural Science Foundation of China (52174283).

Data Availability Statement: The data that support the findings of this study are available from the corresponding author upon reasonable request.

Conflicts of Interest: The authors declare no conflict of interest.

References

1. Tian, J.F.; Yu, L.G.; Xue, R.; Zhuang, S.; Shan, Y.L. Global low-carbon energy transition in the post-COVID-19 era. *Appl. Energy* **2022**, *307*, 118205. [CrossRef]
2. Kittner, N.; Lill, F.; Kammen, D.M. Energy storage deployment and innovation for the clean energy transition. *Nat. Energy* **2017**, *2*, 17125. [CrossRef]
3. Chien, F.S.; Kamran, H.W.; Albashar, G.; Iqbal, W. Dynamic planning, conversion, and management strategy of different renewable energy sources: A sustainable solution for severe energy crises in emerging economies. *Int. J. Hydrogen Energy* **2021**, *46*, 7745–7758. [CrossRef]
4. Lin, Z.M.; Zhang, B.B.; Guo, H.Y.; Wu, Z.Y.; Zou, H.Y.; Yang, J.; Wang, Z.L. Super-robust and frequency-multiplied triboelectric nanogenerator for efficient harvesting water and wind energy. *Nano Energy* **2019**, *64*, 103908. [CrossRef]
5. Sahu, B.K. A study on global solar PV energy developments and policies with special focus on the top ten solar PV power producing countries. *Renew. Sustain. Energy Rev.* **2015**, *43*, 621–634. [CrossRef]
6. Wang, X.S.; Zheng, Y.; Sheng, W.C.; Xu, Z.C.; Jaroniec, M.; Qiao, S.Z. Strategies for design of electrocatalysts for hydrogen evolution under alkaline conditions. *Mater. Today* **2020**, *36*, 125–138. [CrossRef]
7. Dawood, F.; Anda, M.; Shafiuuiiah, G.M. Hydrogen production for energy: An overview. *Int. J. Hydrogen Energy* **2020**, *45*, 3847–3869. [CrossRef]
8. Zhang, X.Y.; Li, F.T.; Dong, Y.W.; Dai, F.N.; Liu, C.G.; Chai, Y.M. Dynamic anion regulation to construct S-doped FeOOH realizing 1000 mA cm⁻²-level-current-density oxygen evolution over 1000 h. *Appl. Catal. B Environ.* **2022**, *315*, 121571. [CrossRef]
9. Yue, M.L.; Lambert, H.; Pahon, E.; Roche, R.; Jemei, S.; Hissel, D. Hydrogen energy systems: A critical review of technologies, applications, trends and challenges. *Renew. Sustain. Energy Rev.* **2021**, *146*, 111180. [CrossRef]
10. Zhang, L.Y.; Zheng, Y.J.; Wang, J.C.; Geng, Y.; Zhang, B.; He, J.J.; Xue, J.M.; Frauenheim, T.; Li, M. Ni/Mo Bimetallic-oxide-derived heterointerface-rich sulfide nanosheets with Co-doping for efficient alkaline hydrogen evolution by boosting volmer reaction. *Small* **2021**, *17*, 2006730. [CrossRef] [PubMed]

11. Surendran, S.; Jesudass, S.C.; Janani, G.; Kim, J.Y.; Lim, Y.; Park, J.; Han, M.K.; Cho, I.S.; Sim, U. Sulphur assisted nitrogen-rich CNF for improving electronic interactions in Co-NiO heterostructures toward accelerated overall water splitting. *Adv. Mater. Technol.* **2022**. [[CrossRef](#)]
12. Janani, G.; Surendran, S.; Choi, H.; An, T.Y.; Han, M.K.; Song, S.J.; Park, W.; Kim, J.K.; Sim, U. Anchoring of Ni₁₂P₅ microbricks in nitrogen- and phosphorus-enriched carbon frameworks: Engineering bifunctional active sites for efficient water-splitting systems. *ACS Sustain. Chem. Eng.* **2022**, *10*, 1182–1194. [[CrossRef](#)]
13. Jiang, Y.Y.; Dong, K.; Lu, Y.Z.; Liu, J.W.; Chen, B.; Song, Z.Q.; Niu, L. Bimetallic oxide coupled with B-doped graphene as highly efficient electrocatalyst for oxygen evolution reaction. *Sci. China Mater.* **2020**, *63*, 1247–1256. [[CrossRef](#)]
14. Du, J.; Li, F.; Sun, L.C. Metal organic frameworks and their derivatives as electrocatalysts for the oxygen evolution reaction. *Chem. Soc. Rev.* **2021**, *50*, 2663–2695. [[CrossRef](#)]
15. Radwan, A.; Jin, H.H.; He, D.P.; Mu, S.C. Design Engineering, Synthesis Protocols, and Energy Applications of MOF-Derived Electrocatalysts. *Nano-Micro Lett.* **2021**, *13*, 132. [[CrossRef](#)]
16. Fan, R.Y.; Xie, J.Y.; Yu, N.; Chai, Y.M.; Dong, B. Interface design and composition regulation of cobalt-based electrocatalysts for oxygen evolution reaction. *Int. J. Hydrogen Energy* **2022**, *47*, 10547–10572. [[CrossRef](#)]
17. Hu, Y.D.; Luo, G.; Wang, L.G.; Liu, X.K.; Qu, Y.T.; Zhou, Y.S.; Zhou, F.Y.; Li, Z.J.; Li, Y.F.; Yao, T.; et al. Single Ru atoms stabilized by hybrid amorphous/crystalline FeCoNi layered double hydroxide for ultraefficient oxygen evolution. *Adv. Energy Mater.* **2021**, *11*, 2002816. [[CrossRef](#)]
18. Zhou, S.Z.; Jang, H.S.; Qin, Q.; Li, Z.J.; Kim, M.G.; Li, C.; Liu, X.E.; Cho, J. Three-dimensional hierarchical Co(OH)F nanosheet arrays decorated by single-atom Ru for boosting oxygen evolution reaction. *Sci. China Mater.* **2021**, *64*, 1408–1417. [[CrossRef](#)]
19. Xi, G.G.; Zuo, L.; Li, X.; Jin, Y.; Li, R.; Zhang, T. In-situ constructed Ru-rich porous framework on NiFe-based ribbon for enhanced oxygen evolution reaction in alkaline solution. *J. Mater. Sci. Technol.* **2021**, *70*, 197–204. [[CrossRef](#)]
20. Cai, C.; Wang, M.Y.; Han, S.B.; Wang, Q.; Zhang, Q.; Zhu, Y.M.; Yang, X.M.; Wu, D.J.; Zu, X.T.; Sterbinsky, G.E.; et al. Ultrahigh oxygen evolution reaction activity achieved using Ir single atoms on amorphous CoO_x nanosheets. *ACS Catal.* **2021**, *11*, 123–130. [[CrossRef](#)]
21. She, L.A.; Zhao, G.Q.; Ma, T.Y.; Chen, J.; Sun, W.P.; Pan, H.G. On the durability of Iridium-based electrocatalysts toward the oxygen evolution reaction under acid environment. *Adv. Funct. Mater.* **2022**, *32*, 2108465. [[CrossRef](#)]
22. Shi, Z.X.; Zhao, J.W.; Li, C.F.; Xu, H.; Li, G.R. Fully exposed edge/corner active sites in Fe substituted-Ni(OH)(2) tube-in-tube arrays for efficient electrocatalytic oxygen evolution. *Appl. Catal. B Environ.* **2021**, *298*, 120559. [[CrossRef](#)]
23. Trotochaud, L.; Young, S.L.; Ranney, J.K.; Boettcher, S.W. Nickel-Iron oxyhydroxide oxygen-evolution electrocatalysts: The role of intentional and incidental iron incorporation. *J. Am. Chem. Soc.* **2014**, *136*, 6744–6753. [[CrossRef](#)] [[PubMed](#)]
24. Friebel, D.; Louie, M.W.; Bajdich, M.; Sanwald, K.E.; Cai, Y.; Wise, A.M.; Cheng, M.J.; Sokaras, D.; Weng, T.C.; Alonso-Mori, R.; et al. Identification of highly active Fe sites in (Ni,Fe)OOH for electrocatalytic water splitting. *J. Am. Chem. Soc.* **2015**, *137*, 1305–1313. [[CrossRef](#)] [[PubMed](#)]
25. Anantharaj, S.; Kundu, S.; Noda, S. “The Fe Effect”: A review unveiling the critical roles of Fe in enhancing OER activity of Ni and Co based catalysts. *Nano Energy* **2021**, *80*, 105514. [[CrossRef](#)]
26. Hu, C.J.; Hu, Y.F.; Fan, C.H.; Yang, L.; Zhang, Y.T.; Li, H.X.; Xie, W. Surface-enhanced raman spectroscopic evidence of key intermediate species and role of NiFe dual-catalytic center in water oxidation. *Angew. Chem. Int. Ed.* **2021**, *60*, 19774–19778. [[CrossRef](#)]
27. Wang, Y.Y.; Qiao, M.; Li, Y.F.; Wang, S.Y. Tuning surface electronic configuration of NiFe LDHs nanosheets by introducing cation vacancies (Fe or Ni) as highly efficient electrocatalysts for oxygen evolution reaction. *Small* **2018**, *14*, 1800136. [[CrossRef](#)]
28. Fan, R.Y.; Xie, J.Y.; Liu, H.J.; Wang, H.Y.; Li, M.X.; Yu, N.; Luan, R.N.; Chai, Y.M.; Dong, B. Directional regulating dynamic equilibrium to continuously update electrocatalytic interface for oxygen evolution reaction. *Chem. Eng. J.* **2022**, *431*, 134040. [[CrossRef](#)]
29. Louie, M.W.; Bell, A.T. An investigation of thin-film Ni-Fe oxide catalysts for the electrochemical evolution of oxygen. *J. Am. Chem. Soc.* **2013**, *135*, 12329–12337. [[CrossRef](#)]
30. Farhat, R.; Dhainy, J.H.; Halaoui, L.I. OER catalysis at activated and codeposited NiFe-oxo/hydroxide thin films is due to postdeposition surface-Fe and is not sustainable without Fe in solution. *ACS Catal.* **2020**, *10*, 20–35. [[CrossRef](#)]
31. Chang, J.L.; Chen, L.M.; Zang, S.Q.; Wang, Y.F.; Wu, D.P.; Xu, F.; Gao, Z.Y. The effect of Fe(III) cations in electrolyte on oxygen evolution catalytic activity of Ni(OH)(2) electrode. *J. Colloid Interface Sci.* **2020**, *569*, 50–56. [[CrossRef](#)]
32. Fan, R.Y.; Zhang, X.Y.; Yu, N.; Wang, F.G.; Zhao, H.Y.; Liu, X.; Lv, Q.X.; Liu, D.P.; Chai, Y.M.; Dong, B. Rapid “self-healing” behavior induced by chloride anions to renew the Fe–Ni(oxy)hydroxide surface for long-term alkaline seawater electrolysis. *Inorg. Chem. Front.* **2022**, *9*, 4216–4224. [[CrossRef](#)]
33. Gao, M.R.; Sheng, W.C.; Zhuang, Z.B.; Fang, Q.R.; Gu, S.; Jiang, J.; Yan, Y.S. Efficient water oxidation using nanostructured α-nickel-hydroxide as an electrocatalyst. *J. Am. Chem. Soc.* **2014**, *136*, 7077–7084. [[CrossRef](#)]
34. Xu, Q.C.; Hua, J.; Zhang, H.X.; Hu, Y.J.; Li, C.Z. Heterogeneous interface engineered atomic configuration on ultrathin Ni(OH)(2)/Ni₃S₂ nanoforests for efficient water splitting. *Appl. Catal. B Environ.* **2019**, *242*, 60–66. [[CrossRef](#)]
35. Wang, J.; Gan, L.Y.; Zhang, W.Y.; Peng, Y.C.; Yu, H.; Yan, Q.Y.; Wang, X. In situ formation of molecular Ni-Fe active sites on heteroatom-doped graphene as a heterogeneous electrocatalyst toward oxygen evolution. *Sci. Adv.* **2018**, *4*, 7970. [[CrossRef](#)]

36. Yi, L.Y.; Niu, Y.L.; Feng, B.M.; Zhao, M.; Hu, W.H. Simultaneous phase transformation and doping via a unique photochemical–electrochemical strategy to achieve a highly active Fe-doped Ni oxyhydroxide oxygen evolution catalyst. *J. Mater. Chem. A* **2021**, *9*, 4213–4220. [[CrossRef](#)]
37. Cheng, X.D.; Yuan, J.X.; Cao, J.H.; Lei, C.J.; Yang, B.; Li, Z.J.; Zhang, X.W.; Yuan, C.; Lei, L.C.; Hou, Y. Strongly coupling of amorphous/crystalline reduced FeOOH/ α -Ni(OH)₂ heterostructure for extremely efficient water oxidation at ultra-high current density. *J. Colloid Interface Sci.* **2020**, *579*, 340–346. [[CrossRef](#)]
38. Liu, Z.R.; Deng, Y.W.; Wang, L.; Tang, J.N. A Facile topochemical preparation of Ni-Fe LDH nanosheets array on nickel foam using in situ generated Ni²⁺ for electrochemical oxygen evolution. *J. Electrochem. Soc.* **2020**, *167*, 046502-9. [[CrossRef](#)]
39. He, W.J.; Ren, G.; Li, Y.; Jia, D.B.; Li, S.Y.; Cheng, J.N.; Liu, C.C.; Hao, Q.Y.; Zhang, J.; Liu, H. Amorphous nickel–iron hydroxide films on nickel sulfide nanoparticles for the oxygen evolution reaction. *Catal. Sci. Technol.* **2020**, *10*, 1708–1713. [[CrossRef](#)]
40. Liu, Y.K.; Jiang, S.; Li, S.J.; Zhou, L.; Li, Z.H.; Li, J.M.; Shao, M.F. Interface engineering of (Ni, Fe)S₂@MoS₂ heterostructures for synergetic electrochemical water splitting. *Appl. Catal. B* **2019**, *247*, 107–114. [[CrossRef](#)]
41. Liu, G.P.; Wang, B.; Wang, L.; Wei, W.X.; Quan, Y.; Wang, C.T.; Zhu, W.S.; Li, H.M.; Xia, J.X. MOFs derived FeNi₃ nanoparticles decorated hollow N-doped carbon rod for high-performance oxygen evolution reaction. *Green Energy Environ.* **2022**, *7*, 423–431. [[CrossRef](#)]
42. Wang, Y.; Zheng, P.; Li, M.X.; Li, Y.R.; Zhang, X.; Chen, J.; Fang, X.; Liu, Y.J.; Yuan, X.L.; Dai, X.P.; et al. Interfacial synergy between dispersed Ru sub-nanoclusters and porous NiFe layered double hydroxide on accelerated overall water splitting by intermediate modulation. *Nanoscale* **2020**, *12*, 9669–9679. [[CrossRef](#)]
43. Chandrasekaran, N.; Muthusamy, S. Free-standing porous interconnects of Ni–Fe alloy decorated reduced graphene oxide for oxygen evolution reaction. *Langmuir* **2017**, *33*, 2–10. [[CrossRef](#)] [[PubMed](#)]
44. Dai, W.J.; Zhu, Y.A.; Ye, Y.K.; Pan, Y.; Lu, T.; Huang, S.F. Electrochemical incorporation of heteroatom into surface reconstruction induced Ni vacancy of Ni_xO nanosheet for enhanced water oxidation. *J. Colloid Interface Sci.* **2022**, *608*, 3030–3039. [[CrossRef](#)] [[PubMed](#)]
45. Hatami, E.; Toghraei, A.; Darband, G.B. Electrodeposition of Ni–Fe micro/nano urchin-like structure as an efficient electrocatalyst for overall water splitting. *Int. J. Hydrogen Energy* **2021**, *46*, 9394–9405. [[CrossRef](#)]
46. Yang, Y.Y.; Meng, H.X.; Kong, C.; Yan, S.H.; Ma, W.X.; Zhu, H.; Ma, F.Q.; Wang, C.J.; Hu, Z.A. Heterogeneous Ni₃S₂@FeNi₂S₄@NF nanosheet arrays directly used as high efficiency bifunctional electrocatalyst for water decomposition. *J. Colloid Interface Sci.* **2021**, *599*, 300–312. [[CrossRef](#)] [[PubMed](#)]
47. Zhu, S.S.; Lei, J.L.; Wu, S.M.; Liu, L.; Chen, T.M.; Yuan, Y.; Ding, C. Construction of Fe-Co-Ni-S-x/NF nanomaterial as bifunctional electrocatalysts for water splitting. *Mater. Lett.* **2022**, *311*, 131549. [[CrossRef](#)]